JGR Space Physics

RESEARCH ARTICLE
10.1029/2021JA029428

This article is a companion to Soret et al. (2021), https://doi.org/10.1029/2021JA029495.

Key Points:

- Mars Atmosphere and Volatile Evolution (MAVEN)/Imaging UltraViolet Spectrograph (IUVS) has detected hundreds of transient, patchy auroral emission events at Mars, mostly near strong crustal magnetic fields
- Events are triggered in evening hours during favorable orientations of the interplanetary magnetic field, and may last for hours
- Visible counterparts to the ultraviolet emissions could potentially be imaged by spacecraft and eventually seen by astronauts

Correspondence to:
N. M. Schneider,
nick.schneider@lasp.colorado.edu

Citation:
Schneider, N. M., Milby, Z., Jain, S. K., Gérard, J.-C., Soret, L., Brain, D. A., et al. (2021). Discrete aurora on Mars: Insights into their distribution and activity from MAVEN/IUVS observations. *Journal of Geophysical Research: Space Physics*, *126*, e2021JA029428. https://doi.org/10.1029/2021JA029428

Received 28 APR 2021
Accepted 31 AUG 2021

Discrete Aurora on Mars: Insights Into Their Distribution and Activity From MAVEN/IUVS Observations

N. M. Schneider[1], Z. Milby[1], S. K. Jain[1], J.-C. Gérard[2], L. Soret[2], D. A. Brain[1], T. Weber[3], Z. Girazian[4], J. McFadden[5], J. Deighan[1], and B. M. Jakosky[1]

[1]Laboratory for Atmospheric and Space Physics, University of Colorado Boulder, Boulder, CO, USA, [2]STAR Institute, University of Liège, Liège, Belgium, [3]NASA Goddard Space Flight Center, Greenbelt, MD, USA, [4]Department of Physics and Astronomy, University of Iowa, Iowa City, IA, USA, [5]Space Sciences Laboratory, University of California, Berkeley, CA, USA

Abstract Mars Atmosphere and Volatile Evolution (MAVEN)'s Imaging Ultraviolet Spectrograph has identified 278 occurrences of discrete aurora events on Mars, which are patchy, sporadic ultraviolet emissions emanating from the upper atmosphere. We confirm prior results finding that emissions are highly correlated with crustal magnetic fields results, with the brightest and most frequent occurrences located around strong crustal fields in the southern hemisphere. The six-year data set shows that events can also occur globally, in regions of weak or absent crustal fields. We find that events occur primarily in evening hours, especially during favorable orientations of the interplanetary magnetic field. Under these conditions, auroral events probably occur nightly and last for hours. Optical counterparts to these UV emissions would probably be detectable with present-day instrumentation, and would be visible to future astronauts.

Plain Language Summary Mars has an unusual magnetic field: it lacks a global field but retains the vestiges of an ancient field locked in regions of the crust. These fields are sufficient to focus charged particle precipitation into the atmosphere and cause aurora. The Mars Atmosphere and Volatile Evolution (MAVEN) spacecraft carries an ultraviolet instrument capable of mapping aurora emissions and correlating them with conditions that favor aurora. We have detected hundreds of auroral events allowing the first statistical study of their behavior. We find that events occur primarily in evening hours, especially during favorable orientations of the interplanetary magnetic field. Under these conditions, auroral events probably occur nightly and last for hours. Astronauts, whenever they reach Mars, would have a good chance to see this natural wonder from above or below.

1. Introduction

The Mars Atmosphere and Volatile Evolution (MAVEN) spacecraft has been orbiting Mars since September 21, 2014, with a primary mission to study the behavior of the upper atmosphere and the escape of its constituent gases to space (Jakosky et al., 2014). At the time of these observations, MAVEN orbited Mars on a 4.5-h elliptical orbit with a closest approach to Mars' surface at periapse of 150–200 km and an apoapse ranging from 6,200 km to 4,400 km over the mission. MAVEN carries one remote sensing instrument for the study of Mars' upper atmosphere: the Imaging UltraViolet Spectrograph (IUVS) (McClintock et al., 2015). The instrument captures spectra of the planet and its atmosphere in the far-UV (FUV) from 110 to 190 nm and mid-UV (MUV) from 180 to 340 nm, ideal for recording well-known atmospheric emissions from CO_2 and its dissociation and ionization products. The instrument is mounted on an Articulated Payload Platform (APP), which can orient IUVS's field of view relative to Mars depending on spacecraft location, orientation and desired viewing geometry. IUVS was designed to observe the Mars dayglow, nightglow, hydrogen corona, D/H ratio, and stellar occultations, and is also sensitive to auroral emissions.

Mars exhibits at least three types of aurora (Figure 1). The SPICAM instrument on Mars Express discovered discrete aurora: small, short-lived patches of aurora related to the crustal magnetic fields in Mars' southern hemisphere (Bertaux et al., 2005). MAVEN/IUVS discovered a second type called diffuse aurora (Schneider, Deighan, Jain, et al., 2015 [hereafter Schneider15]; Jakosky et al., 2015; Schneider et al., 2018, hereafter Schneider18), with emissions spanning much of Mars' nightside. Diffuse aurora are attributed to solar energetic

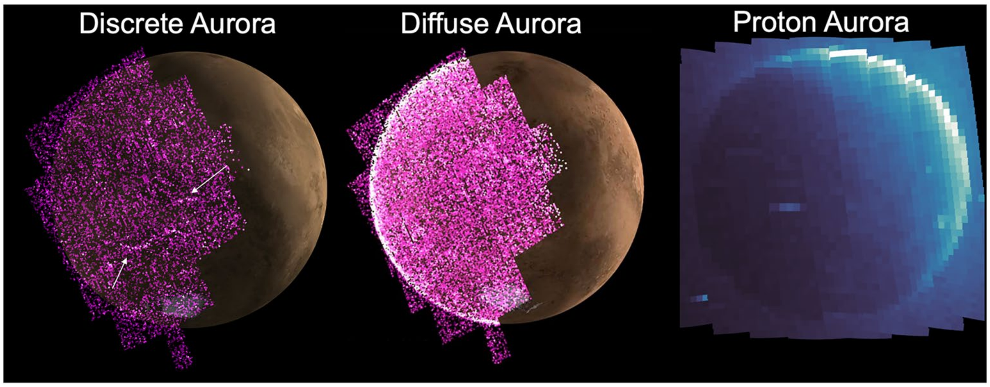

Figure 1. Three types of aurora on Mars. Mars Atmosphere and Volatile Evolution (MAVEN)/Imaging UltraViolet Spectrograph (IUVS) apoapse images from orbits 5738, 5831, and 849.

particles (SEPs), specifically electrons or protons accelerated to energies of ~100 keV. MAVEN/IUVS also discovered a third form called proton aurora occurring on Mars' dayside, caused by penetrating protons from the solar wind (Deighan et al., 2018; Halekas et al., 2017; Ritter et al., 2018).

The SPICAM discovery of discrete aurora was based on three ultraviolet emissions in the Cameron bands (the $a^3\Pi$–$X^1\Sigma$ transition of CO from 190 to 270 nm), the ultraviolet doublet or UVD (the $B^2\Sigma_u^+$–$X^2\Pi_g$ CO_2^+ transition at 289 nm), and the oxygen forbidden emission at 297.2 nm (Bertaux et al., 2005). These can all be generated by electron impact on CO_2, similar to their generation on Mars' dayside initiated by solar extreme ultraviolet (EUV) flux and photoelectrons. Subsequent work (Gérard et al., 2015; Leblanc et al., 2006, 2008; Soret et al., 2016) expanded the list of known events to 19 spanning SPICAM's decade of observation. 16 of these detections were in nadir viewing, and only three in limb viewing as employed in this study. Gérard et al. (2015) also found the duration of events to be in the range of seconds to tens of seconds, though the lack of repeated observations prevented a study of recurrence rates. They also compared the latitudinal distribution of the auroral events observed at nadir with concurrent measurements of the electron energy spectra measured with the ASPERA-3 instrument on board Mars Express. They showed that the auroral events were correlated with locations of increased precipitated energy flux, but were not necessarily vertically aligned with the UV aurora, suggesting that the magnetic field lines threading the aurora could be significantly tilted. Soret et al. (2016) found that the brightness of the discrete aurora was not proportional to the precipitated energy flux, a possible indication that the electron flux was modified between the altitude of the spacecraft and the atmosphere.

SPICAM detections were found to be correlated with crustal field structures based on overplotting the detections on a crustal magnetic field map (Brain et al., 2007; Figure 5). This map displays the probability of open field lines at 400 km altitude as measured through electron distributions from Mars Global Surveyor. The measurements were made consistently around 2 a.m. local time on Mars' nightside due to the fixed orbit of the spacecraft (In the figures below, we also make extensive use of this map for context. The original map uses a rainbow colormap, but we have replotted the map data with a subdued blue-white colormap in order to allow multiple types of data to be clearly overplotted.)

The properties of the precipitating population have been studied by contemporaneous charged particle measurements (Brain, Halekas, et al., 2006; Gérard et al., 2015; Leblanc et al., 2006, 2008) and modeling of energy deposition and resultant emission (Leblanc et al., 2006; Soret et al., 2016). Taken together, they point to an accelerated electron population in the range of 40–200 eV depositing their energy around 135 km altitude.

More than a decade later, MAVEN/IUVS obtained the first images of discrete aurora, confirming their alignment with regions of magnetic fields likely to be open to space (Schneider18). MAVEN's Solar Wind Electron Analyzer (SWEA) has also measured electron energy and pitch angle distributions to examine more deeply the accelerated electron populations associated with discrete aurora (Xu et al., 2020).

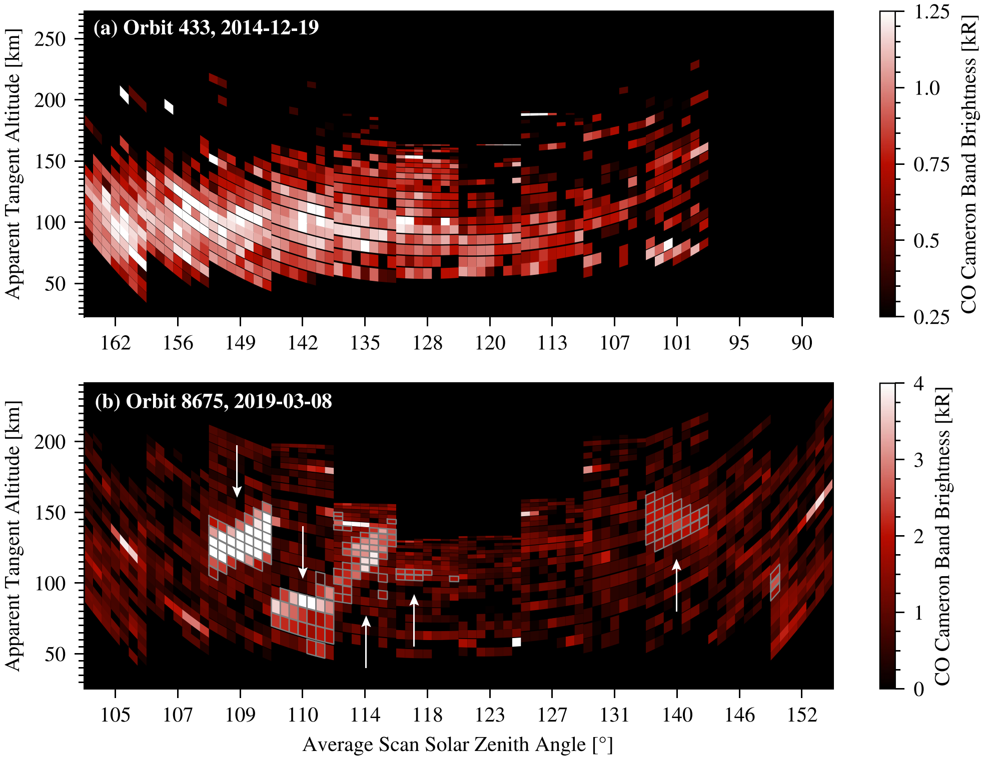

Figure 2. Mid-ultraviolet composite limb scan images of two types of Mars aurora, with diffuse aurora at the top and discrete aurora below. The red-to-white colormap displays the intensity of the CO Cameron band emission excited by particle precipitation. Imaging UltraViolet Spectrograph (IUVS) scanned its slit vertically through the atmosphere 12 times, while the spacecraft traveled horizontally near periapse from left to right. The data are shown contiguously in rectilinear format even though the sampled regions are non-contiguous. In the top image, emission is fairly uniformly enhanced along the entire observation period at a characteristic limb altitude. In the bottom image, emission is patchy but pixels with statistically significant aurora detections are outlined in gray and confirmed auroral events are identified by arrows. Bright pixels away from auroral patches are caused by cosmic rays.

Despite 15 years of study, many fundamental questions about discrete aurora remain:

- How are discrete aurora events distributed over Mars surface? Can events occur in regions devoid of crustal fields?
- What is the occurrence frequency of auroral events? Do some locations exhibit frequent, repeatable or long-lasting aurora?
- Can emission brightnesses and other spectral properties be used diagnostically on the excitation, emission, or radiative transfer processes?
- What conditions lead to the precipitation causing auroral emissions? Are there preferred local times or magnetospheric indicators such as the interplanetary magnetic field (IMF)?

This paper focusses on the detection and characterization of discrete aurora events, their geographic distributions and occurrence frequency. A companion paper (Soret et al., 2021, hereafter Soret21) addresses the spectral properties and vertical profiles and performs case studies using electron precipitation data.

2. Observation and Analysis Methods

The observations described herein captured discrete aurora emissions in limb scans during MAVEN's periapse passes, similar to observations used for the study of dayglow (Jain et al., 2015; Schneider, Deighan, Stewart, et al., 2015), diffuse aurora (Schneider15) and nightglow (Stiepen et al., 2017). Figure 2 illustrates how the discrete aurora phenomenon is distinct from diffuse aurora. They are spectrally similar, apart from the relative strengths of emission features, but are fundamentally different spatially and temporally. Diffuse aurora is spatially homogeneous and continuous over thousands of kilometers, and usually appears at apparent altitudes of 100 km or below. Its near-uniformity suggests the projection of emission against the limb reasonably approximates the altitude structure of emission. Discrete aurora events are discontinuous from scan to scan and even within a scan. The nonuniform distribution suggests incomplete coverage of the planet, meaning patches of emission do not generally lie at the limb. The corresponding altitudes must therefore be considered to be projected altitudes, indicating a lower limit on their true altitudes. Below we describe the full data set and methods used to detect discrete aurora events.

2.1. IUVS Limb Scan Observations

Periapse limb scans construct a series of two-dimensional images of atmospheric emissions projected against the sky at the limb. The instrument field of regard, limited by a stray light baffle, looks 90° to the right relative to the spacecraft's motion. The 10° long IUVS slit is maintained parallel to the spacecraft's motion (approximately parallel to the limb), and a scan mirror moves the slit's field-of-view vertically through the atmosphere between ∼50 and ∼200 km tangent altitude. For most observations, a vertical scan consists of 21 exposures of 4.2 s (plus 0.6 s readout time) taking slightly less than two minutes per scan. In a typical periapse pass of 22 min, 12 vertical scans are obtained covering a range of latitudes, longitudes, and local times. During some orbits, 24 scans with 11 vertical positions and exposures times of 4.6 s were obtained to give partial spatial overlap between scans. Later in the mission, 14 scans were obtained during periapse with the same exposure and readout times as the 12-scan orbits. The detector is binned to cover the full MUV spectral range at 256 or 512 spectral element binning for most observations, and each exposure's along-slit information is binned onboard into seven spatial elements. Individual data files contain additional observation details, which indicate exceptions to the default exposure or binning parameters. Note that simultaneous FUV observations were made but are not analyzed in this study.

The observation files used in this work are identified as "periapse" version 13 of the Level 1B data available at the PDS IUVS repository under "Limb Scan … Processed Data." The data processing methodology for nightside observations is described in detail in Schneider et al. (2020). Below we describe additional processing steps unique to this auroral study. The specialized data products described below to identify and characterize discrete aurora have been placed in a FAIR repository as described in the Acknowledgments.

Nightside spectra consist primarily of emissions from aurora and nitric oxide (NO) nightglow, though solar continuum can contaminate the spectrum near the terminator. To isolate the auroral emission brightness, we use a multilinear regression technique (MLR) to fit the observed spectrum of each spatial pixel (Stevens et al., 2015). The method is functionally equivalent to that used by Schneider15, including the use of identical templates and spectral ranges. We used templates derived from IUVS observations isolating the individual spectral components including auroral emissions (the CO Cameron bands, the CO_2^+ UVD emission and the O I forbidden transition) as well as NO nightglow (184–276 nm) and solar continuum. The fit also includes a constant term indicating the presence of elevated background or other instrumental artifacts. The resulting full nightside data uses observations from orbit 335 (December 1, 2014) through orbit 11484 (May 7, 2020) containing 57,259 vertical scans from 4,566 orbits with a total of 8,119,468 independent spatial pixels.

The instrumental fitted spectra were converted to kiloRayleighs (abbreviated kR) per nm using stellar calibration observations (Schneider et al., 2020), and then summed over the spectral feature to yield the emission brightness in kR. Random uncertainties in a pixel's fitted intensities were calculated based on the combination of photon statistics and detector background noise in the original spectrum. Uncertainties on the per-pixel fitted intensities were validated by measuring fit residuals related to the spectral template.

2.2. Auroral Detection Methodology

Detection of auroral events proceeded in three phases. First, the entire nightside data set was filtered to eliminate observations on the dayside or within 15° of the terminator (solar zenith angle <105°), with instrumental defects such as cosmic rays, incomplete altitude range or during previously identified solar energetic particle events (particularly the space weather events analyzed in Schneider15; Jakosky et al., 2015, Schneider18). This yielded a total of 4,044,523 spatial pixels in 33,319 scans over 4,220 orbits for further examination.

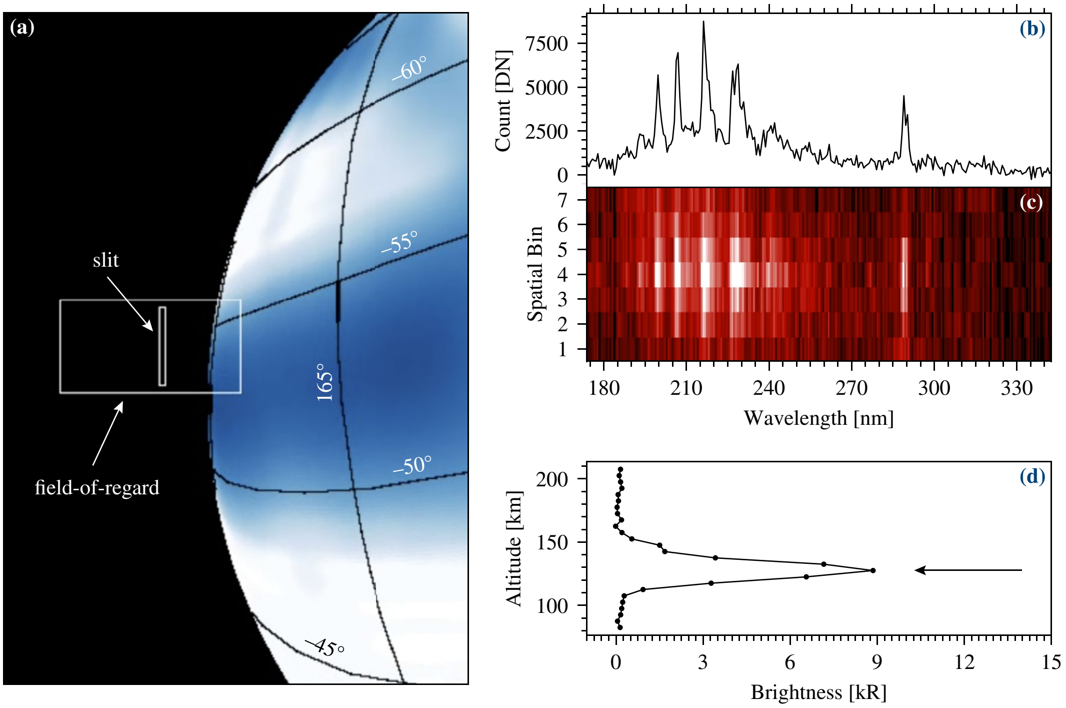

Figure 3. Sample detection of a discrete auroral event in Orbit 8675, Scan 3, Integration 12. (a) Observing geometry showing a portion of the Mars globe mapped with the probability of closed field lines (with blue indicating higher probability of open field lines; see Figure 5). Spacecraft motion is downwards in the image. (b) Line plot of the integrated spectrum within the slit, with integrated Cameron band brightness 5.7 ± 0.1 kR. (c) Spatially resolved spectrum showing emission peaked at slit center. (d) Vertical intensity profile of Cameron band emission from the entire scan is shown at lower right, with an arrow indicating the location where the spectrum was obtained.

Second, each spatial pixel's CO Cameron band emission was tested for statistical significance. All pixels in a scan with CO Cameron band signal-to-noise ratio (SNR) > 4 or CO_2^+ UVD signal-to-noise ratio >3 were averaged to yield a composite spectrum and Pearson R correlation coefficients with the Cameron band fitted template between 190 and 246 nm were computed. Scans containing more than three statistically significant pixels with $R > 0.55$ were deemed potential detections. This winnowed the data set to 10,392 pixels in 794 scans across 520 orbits. We note that this automatic detection step is efficient but cannot identify or optimize all plausible auroral event detections. For example, low signal-to-noise pixels adjacent to those of higher signal-to-noise are not co-added to boost the final detection, even though they probably contain auroral emission.

Finally, each potential detection's composite spectrum was examined by eye and in context for final approval. Primary reasons for rejection were (a) observations sufficiently close to the terminator that they were visibly affected by solar continuum or scattered dayglow; (b) lack of spatial coherence among the selected bright spatial elements, and (c) contemporaneous solar energetic particle activity known to cause diffuse aurora. This final filtering yielded confirmed detections in 278 scans in 196 orbits using 4,101 spatial pixels. Figure 3 shows a sample confirmed detection in orbit 8675.

For each detection, we tabulated observation parameters, average MUV emission brightnesses with uncertainties, average projected altitudes with vertical standard deviations, tangent point locations and local times. The complete table of detections appears in the FAIR data repository listed in the Acknowledgments. The sensitivity limit for the CO Cameron bands is ~0.5 kR, based on the minimum brightness of detections which pass both the statistical and by-eye tests. For the UVD feature, which is narrower and more sharply peaked, the sensitivity limit is ~0.03 kR. Note that the detection confirmation was performed with the Cameron band and UVD features, but additional fitted brightnesses are provided for other spectral components. UVD brightnesses are reported for ~60% of detections, with much lower values for other emissions.

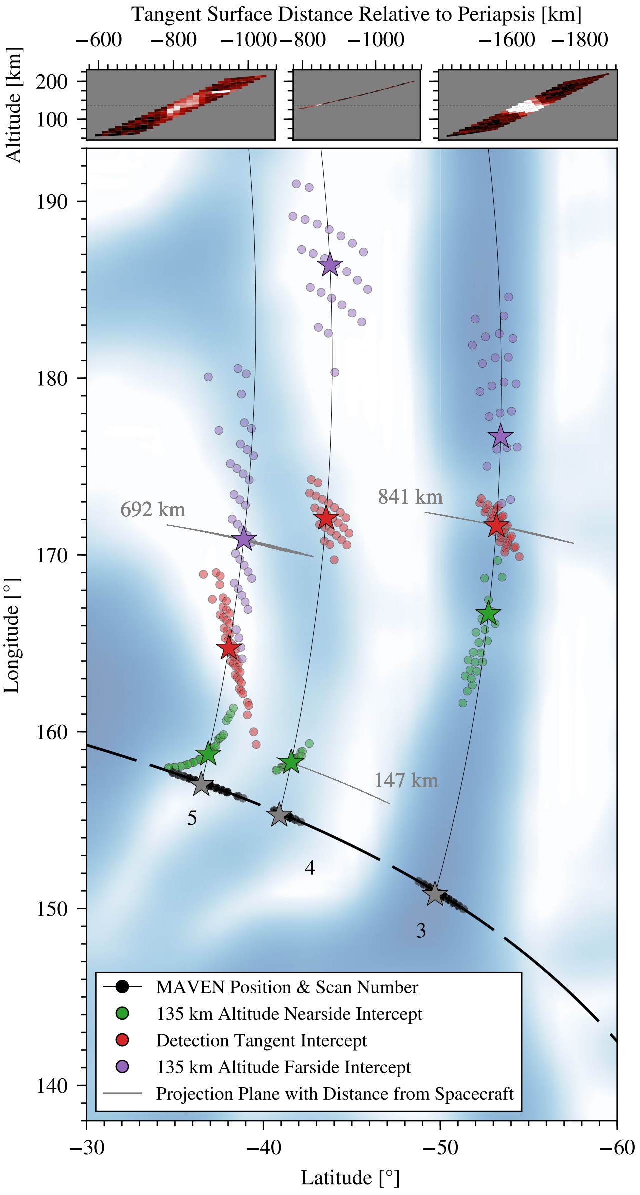

Figure 4. Detection case study for Orbit 8675.The base map shows the probability of closed fields lines. White indicates high values, meaning aurora are more likely to occur in blue "magnetic valleys." The spacecraft ground track appears as a black line, with dots to indicate the location when integrations show confirmed auroral detections. Red dots indicate the sub-tangent locations for these detections. Colored dots show alternate emission locations on the assumption the emission occurs at 135 km either on the nearside (green) or farside (purple) of the limb. Stars in each color represent the spatial centroids of the dots. The images at top show the auroral data projected onto the planes indicated by gray lines intercepting starred locations. The dotted lines across these images indicate the 135 km probable emission altitude.

Much of the detection effort was carried out using graphical "quicklooks" containing plots similar to Figures 2–4 for every detection. These products are available in the FAIR data repository. The vast majority of detections exhibited one or more of the common characteristics of discrete aurora: (a) no identifiable external trigger from solar activity, (b) located in and around crustal magnetic fields, (c) isolated emission in a single scan with no emission in adjacent scans (suggesting limited spatial or temporal extent), (d) nonuniform or tilted morphology within a scan (suggesting patchy structure) and/or (e) low apparent altitude (indicating patchy emission in the foreground or background). These detections carry the flag "probable discrete aurora" in the database. A minority are flagged as "ambiguous," especially those showing detections in multiple scans per orbit resembling diffuse aurora, but without evident external triggers. These are more common in regions of weak or no crustal fields. Given our poor understanding of how discrete aurora work in these regions, we retain these points in the database as candidates for future study. If in the end they are not discrete aurora, they form a "background" that adds some minor confusion to the plots that follow but do not obscure the strong patterns and trends for discrete aurora. In addition to the detections database, the FAIR repository also includes document listing times and locations of all valid observations which can be used to evaluate occurrence frequencies accounting for observation bias. The remainder of the paper focusses on these two datasets.

3. Locations and Morphologies of Auroral Events

Once a detection has been confirmed, it can be analyzed for geographic, spatial and timing information. The interpretation of the emission patch locations and morphologies are complicated by several factors. First, the observations are made from a platform rapidly changing in latitude, longitude and altitude over the 22-min periapse pass. In this time the spacecraft travels roughly 90° around the planet spanning ∼5,000 km at ∼4 km/s. This lateral motion can be significant compared to the vertical motion of the slit, meaning that scan images actually form tilted diamonds instead of rectangles. Second, the spacecraft altitude changes the distance to the limb, hence the spatial scales of the images change. From the maximum altitude of ∼400 km, the limb lies more than 1,000 km away, and spatial pixels subtend large physical dimensions. When the spacecraft reaches the minimum altitude, sometimes as low as ∼120 km, the distance to the limb becomes meaningless, and in fact the spacecraft could be looking up at an auroral patch or even lie within it. Finally, the emission patches do not even generally lie at the limb, and could in principle lie anywhere along the line of sight either in front of the limb or beyond it.

Emission patches lying well below 100 km apparent altitude are especially challenging to interpret due to the ambiguity of their location in front of or behind the limb. Based on the altitude profiles presented in Soret21 and past studies described in the introduction, the probable true altitude of emission is ∼135 km, which significantly simplifies the interpretation in many cases. However, we note that the precipitation and emission processes could easily affect the emission peak altitude by up to 10 km, with significant consequences on attempts to identify the auroral patch locations.

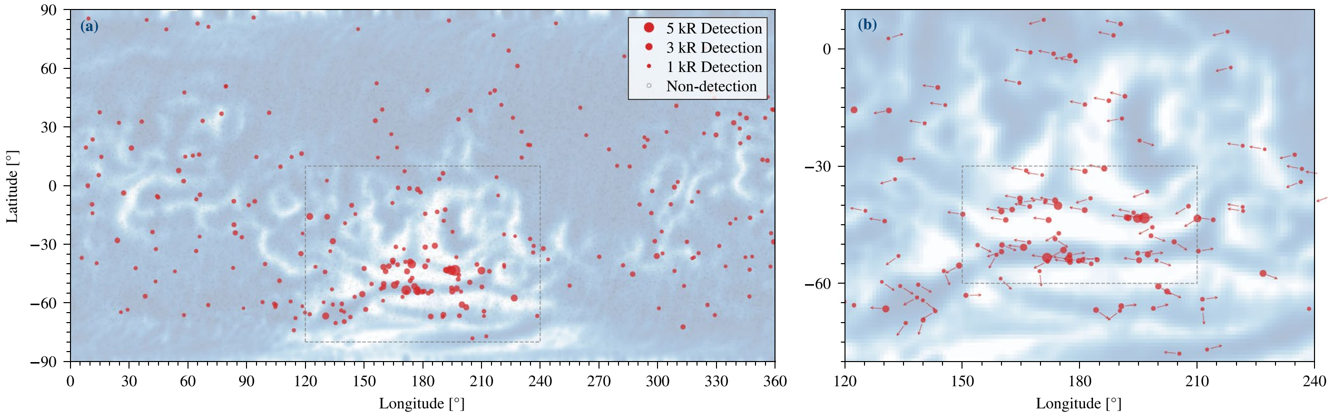

Figure 5. Detection locations and intensities. Detections are shown with red dots whose size scales with Cameron band brightness. Nondetection locations appear in the left panel as faint open circles, so numerous they appear to cover the planet uniformly. Nondetections are omitted in the right panel for clarity. In the right panel, arrows point from the detections toward the spacecraft location at the time of detection. The observational bias for eastward/westward viewing is evident.

Despite the complexities enumerated above, a wealth of insights about each detection can be extracted. We use the case study of detections in Orbit 8675 (as shown previously in Figures 2 and 3) to illustrate. Figure 4 uses a magnetic field base map to indicate the spacecraft ground track and auroral detections in Scans 3, 4, and 5, and plausible visual representations of the appearance of the auroral patches.

These new fiducials allow a closer scan-by-scan examination of probable emission locations. For Scan 3, the green and blue dots lie adjacent to the red dots, indicating the limb approximation is reasonable. For Scan 4, however, the nearside and farside dots are quite far apart, due to the low apparent altitude of emission. In fact, the purple farside points lie about 10 times farther than the nearside points. The fact that the farside points overlie a region of closed crustal fields might argue against this location, a topic we will return to in Section 4.1. For Scan 4, the green star is a more likely location for the emission. For Scan 5, both nearside and farside locations are plausible in terms of magnetic field conditions, but the ambiguity can be resolved when considering the appearance of the emission in the next stage of analysis.

The auroral patch dimensions and morphology are linked to the patch's location relative to the spacecraft, due both to its projection distance and the parallax from spacecraft motion. The smaller the distance, the smaller the dimensions and the larger the parallactic horizontal motion. We use the location possibilities discussed above to create plausible images for the emissions as seen from the spacecraft in the same three scans. Line segments through these starred locations in Figure 4 represent plausible surfaces on which the plane-of-sky emission would be projected.

The top panels in Figure 4 show each image at its selected projection distance. All emissions now peak near 135 km, as expected for the choice of emission location. Scan 4 illustrates the effects of viewing a nearby auroral patch: both spatial dimensions are shrunk, and the slit length is entirely filled with emission that probably extends well past the ends of the slit. The parallactic shift caused by spacecraft motion noticeably increases the tilt of the image. This effect is the reason for rejecting the nearside intercept for Scan 5, based on the emission's narrow structure centered in the slit. If projected instead at the green star's distance, the image would shrink even smaller and become more tilted than Scan 4. It becomes implausible that the slit motion would track the fine structure so perfectly.

The case study from Orbit 8675 quickly demonstrates that each auroral detection would need to be examined individually in light of the observing parameters and magnetic field geometry in order to better locate the emission and determine size and morphology. We save this effort for a later study. For the purposes of this work, we retain and tabulate three potential locations per detection: (a) the subtangent point of the observed emission centroid (red star), along with the apparent altitude of the emission centroid; (b) the location below the nearside 135 km intercept (green star), and (c) the analogous farside 135 km intercept (purple star). Locations of the first type are used in the remainder of the paper. Note that detections with centroid altitude above 135 km cannot have values for 2 and 3. Special cases can similarly invalidate the calculations for alternate locations, e.g., nearside intercepts are not possible when the spacecraft lies below 135 km. We note again that the 135 km intercept choice may not be representative for all events, and small changes in this altitude can lead to substantial displacements in location.

The by-eye examination of each detection flagged a significant number of intriguing cases for follow-up. For example, in Orbit 8681 Scan 5, two distinct emission patches can be seen at different apparent altitudes in a “magnetic valley” adjacent to that in Figure 3. Though the detection algorithm tabulates this as one event, the notes column in the database identifies this type of case for further study. A second interesting and very common class of detections occur near periapse, with slit-filling emission varying little with viewing angle (e.g., Orbit 8604, Scan 7). These are probably cases when the MAVEN spacecraft is extremely close or possibly within the emission patch. These would be ideal cases for studies leveraging MAVEN's simultaneous electron and magnetic field measurements.

4. Observational Results

4.1. Geographic Distribution, Frequency, and Duration of Auroral Events

The summary statistic of 278 detections in 33,319 favorable nightside scans leads to a globally averaged ~0.834% detection rate. This rate is a combination of the natural occurrence rate of the aurora and geometrical considerations beyond our knowledge, such as the overlap between observation locations and magnetic field properties conducive to aurora. This therefore represents a lower limit to the actual occurrence of discrete aurora.

Figure 5 shows the global distribution of auroral detections on the base map of closed field line probability based on Mars Global Surveyor electron data. The most frequent and brightest events occur in the crustal field region indicated by the box in the left panel, and enlarged in the right panel. At center in the right panel are three large regions of closed field lines shown in white nicknamed “the sailboat.” The most intense emissions lie just above and below the body of the boat. A 30° × 60° dotted box in the right panel delineates a reference region of strong crustal fields and bright emissions, which will be used for further statistical analysis.

The strong association of the brightest and most frequent events with the magnetic field map is somewhat surprising. First, the ambiguity of emission location described in Section 3 evidently has little effect on the distribution seen on a global scale. Second, and perhaps more importantly, even the map matches the data better than should be anticipated. The map was obtained from MGS results at 3 a.m. local time, specific to the planet's orientation relative to the interplanetary magnetic field and the solar wind. Shifts in the pattern were expected for different local times, and substantial deviations from this average picture were expected based on highly variable magnetospheric conditions. Neither of these affects seem significant on this scale.

A close look at the full map shows many events outside the strong crustal fields. The majority of those lie near weak crustal fields, which we examine more closely in the next section. Still more appear far from any crustal fields, such as those at southern latitudes on the left and right sides of the global map. This is partly the fault of the cylindrical map's distortion, which exaggerates distances for mid- and polar latitudes, but there are still many detections at large distances from crustal fields that merit deeper investigation.

Figure 6 quantifies the map above by calculating the occurrence rate binned into 30° × 30° bins. High occurrence rates of 3%–5% in the strong crustal field region of Figure 5b are immediately obvious in two light-colored boxes below center. This statistic applies regardless of viewing geometry, so again it represents a lower limit to the actual occurrence rate.

A close examination of repeated observations in the “sailboat” region shows that the occurrence rate for favorable magnetic and observational geometry may approach unity. During Orbits 8615–8693, MAVEN was favorably situated for nightside periapse observations, as in Orbit 8675 from preceding figures. Furthermore, the orbital period was deliberately adjusted to almost exactly to one-sixth of one Mars sol for magnetic field studies. As a result, observing geometry and geographic location repeated nearly identically every six orbits. Between February 26 and March 11, 2019, IUVS obtained 14 nearly identical observations. The primary differences, day-to-day, were slight timing offsets of the scans relative to the crustal fields and very slight longitudinal drifts. Four observations suffered from poor timing, meaning the scans looked too

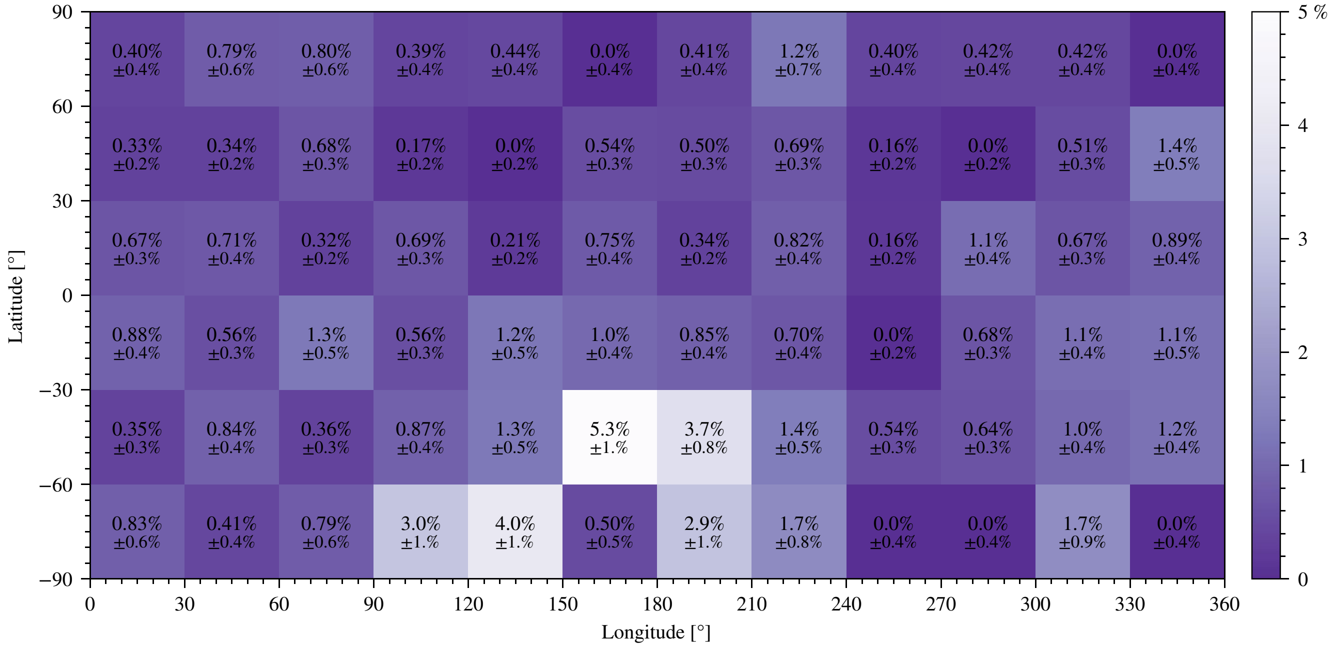

Figure 6. Detection frequency in geographic coordinates. In each bin, the number of detections is divided by the number of favorable observations, which could have detected auroral emission. Uncertainties come from counting statistics, for example, in the lower left corner there were 2 ± 1.4 detections out of 241 observations. The typical number of observations per box ranges from ∼300 in the top and bottom rows to ∼600 elsewhere.

low or too high when centered relative to the crustal fields. In the remaining 10 observations, auroral events were automatically detected and confirmed in 8, giving an occurrence rate of 80% for favorable magnetic and observational geometry. Two non-detections were observed a region farther east than all the others, due to small longitudinal drifts. If this location was in fact not magnetically favorable, then the occurrence rate would be ∼100% from these observations.

Despite the focus of Figures 5 and 6 on the strong crustal field region, they also show that a substantial number of discrete aurora events are actually distributed globally in areas of weak or non-existent crustal fields. While events away from strong crustal fields were less bright, other characteristics such as spectral properties or peak altitude did not differ from those in strong crustal field regions (see Soret21). The lack of clusters or alignments of independent detections outside of strong crustal fields suggest the auroral events are not highly repeatable there.

The scanning nature of IUVS observations helps place a lower limit on the duration of auroral events. The vast majority of bright events show coherent structure over 5–10 adjacent integrations of ∼5 s each (see Figure 2), suggesting durations of at least tens of seconds. There are no instances of bright emission within a single 5-s integration bracketed by integrations without any auroral signal (Due to the lack of overlapping scans, it is not possible to estimate an upper limit to event durations.). The ≥80% repeatability of detections in the 8615–8693 orbit range discussed above also makes a strong case that events would occur nearly nightly and potentially last for hours in the most favorable magnetic and viewing geometry. The high repeatability of IUVS limb scans at first seems at odds with SPICAM's non-repeatability in nadir viewing. These two results can be reconciled if emissions take the form of small patches that move along the "magnetic valley," as opposed to filling the entire valley through the evening hours.

4.2. Correlation With Crustal Field Strength

Figure 7 shows in greater detail the dependence of auroral occurrence frequency on crustal fields. A new crustal field strength map based on low-altitude MAVEN measurements obtained below 250 km (Weber, 2020) is used to assign a radial field strength value B_r to each IUVS observation, both detections and non-detections. Radial fields are their strongest when normal to the surface which correlates with a high

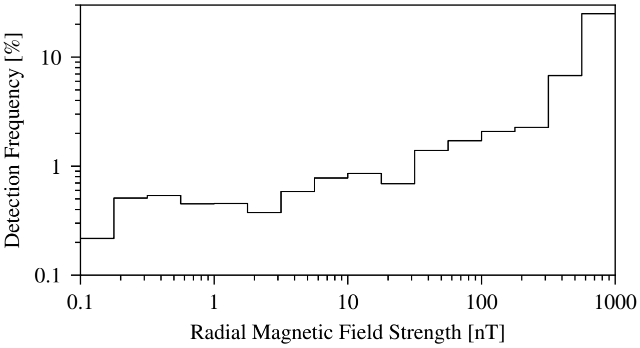

Figure 7. The detection frequency is shown versus radial magnetic field strength. The histograms use logarithmically spaced bins with four bins per decade. Auroral events are 40 times more likely to occur in the highest field regions than most of the rest of the planet, though such regions are rare.

probability of open field lines. The detections are divided by total observations and the results binned logarithmically. In the rightmost bin (>562 nT), there were 32 observations with eight detections from separate orbits. These eight comprise ∼3% of all detections though only 0.08% of the planet exhibits such high field strengths. The likelihood of aurora in regions of the strongest fields is therefore nearly 40 times the planetary average. The trend extends to lower field strengths: for $B_r \geq 30$ nT, we find ∼35% of all events occurring in ∼11% of the planet's area, giving triple the planetary average.

Figure 8 shows the influence of crustal field strength on emission brightness. The brightest events occur in field strengths greater than 30 nT. The flattening of the curve at low values may simply be a result of the detection threshold, as only events brighter than about 0.6 kR pass the SNR test. This limit does not affect the CO_2^+ data, so no change in emission ratio can be inferred from this plot. While the trend for greater brightness with B_r is evident, these data cannot differentiate between increased flux or energy of the precipitating particles.

4.3. Local Time and Interplanetary Magnetic Field Angle Control

Below we describe a search for controlling factors on the occurrence of discrete events, with a focus on the 58 detections in the strong crustal field region. We examined occurrence frequency as a function of local time and interplanetary magnetic field (IMF) clock angle. We first confirmed observations were sufficient for statistical significance and lack of observational bias. At the highest level, we divide local times into pre- and postmidnight halves, and IMF into positive and negative halves. In evening hours, the data set includes 350 observations for negative IMF angles and 308 for positive angle. For post-midnight observations, we have 218 observations for negative IMF angles and 169 for positive angles. We therefore conclude no quadrant of these parameters lacks sufficient observations for statistical significance. As in the sections above, we use detection frequency (detections divided by observations), to normalize for unequal numbers of observations.

Local time analysis finds events are strongly favored in evening hours. Figure 9 shows the 278 detections subdivided into one-hour local time bins, inside and outside the 30° × 60° strong crustal field region (see Figure 5b). Events in the strong crustal field region are strongly controlled by local time, with the vast majority of events taking place in the evening before 22 h local time. While many of these detections did occur in the favorable orbit range 8600–8699 (Section 4.1), the majority of events occurred at other phases of the mission.

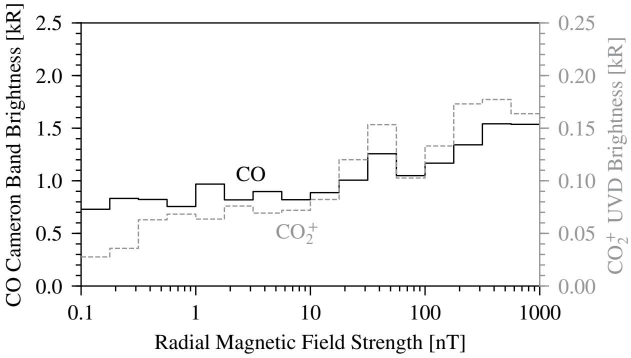

Figure 8. The emission brightness is shown versus radial magnetic field strength. The brightest events occur in field strengths great than 30 nT.

The evening occurrence frequencies in the range 7%–16% are again lower limits on the occurrence of aurora, not accounting for the detailed magnetic field structure within the extended region nor the timing of scans relative to magnetic field structures. The ≥80% repeatability in the Orbit 8600–8699 series results from favorable observing geometry, crustal field geometry, and local time. The aurora in the particular location must be active and detectable nearly continuously throughout the evening, at least when sampled on timescales of tens of seconds.

Discrete aurora detections over the rest of the planet also show an enhancement in the evening hours, but additionally exhibit events over the entire night at a more uniform level. The overall distribution could be a combination of the evening peak seen in the strong crustal field region plus an additional component caused by an excitation process independent of local time. This is plausible because the large spatial sample intermixes regions of medium strength crustal fields and regions with no crustal fields.

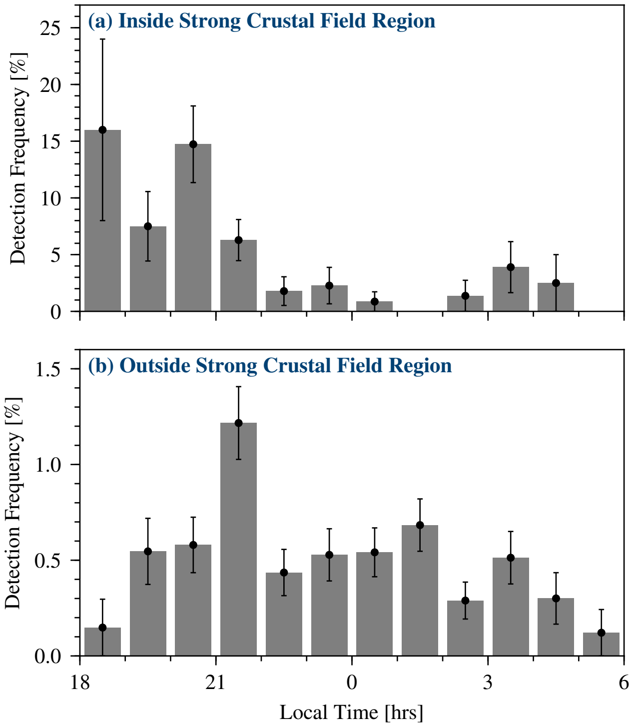

Figure 9. Detection frequency versus local time. Inside the strong crustal field region, nearly all events occurred before 22 h local time. Outside the strong field region, events occur more uniformly over the night. Uncertainties are derived from counting statistics using the number of detections. Local time bins each had ten to hundreds of observations in (a) and hundreds to thousands of observations in (b).

Analysis of IMF orientations also reveals its strong control over discrete aurora. Figure 10 shows the distribution of events with respect to the IMF clock angle of the upstream solar wind (as defined in DiBraccio et al., 2018). The clock angle is positive when the B_y component of the IMF is positive, and negative when B_y component is negative. We derive clock angles using orbit-averaged (Halekas et al., 2017) observations from MAVEN's Magnetometer (Connerney, Espley, DiBraccio, et al., 2015; Connerney, Espley, Lawton, et al., 2015), which measures the components of the IMF during apoapsis segments of MAVEN's orbit. Clock angles clusters near ±90°, corresponding to the "toward" and "away" sectors of the solar wind. At Mars, they alternate with a period of about 13 days (Brain, Mitchell, & Halekas, 2006; Hurley et al., 2018; Wilcox & Ness, 1965). For an event to be assigned a clock angle, the solar wind observation must be within five hours of the aurora detection.

Figure 10a shows that discrete aurora in strong crustal fields regions occur more frequently at negative IMF clock angles than positive ones, with nearly all aurora events inside the crustal field region at negative clock angles. In contrast, Figure 10b shows that the clock angles for aurora events outside the crustal field region show only a slight preference for negative angles.

Combining the local time and IMF results reveal that discrete aurora events inside the crustal field region are much more likely to occur at dusk with negative IMF clock angles. Quantitatively, the detection frequency for "evening + negative IMF" is 9.1% (32 of 350 observations, vs. 0% for "morning and positive IMF" [0 of 169 observations]). 16 detections would have been expected if the 9.1% detection frequency applied for "morning and positive IMF," so the complete lack of detections is significant. The detection frequency for "morning + negative IMF" is 2.8% (6/218), and for "evening + positive IMF," is 1.0% (3/308).

5. Conclusions and Discussion

The wealth of new observations of discrete aurora allows for a deeper level of interpretation than was possible from the original observations by the SPICAM instrument. We start with a phenomenological comparison between this study and prior work, and then discuss the implications of the key observational results on our understanding of how discrete aurora work. The closing section offers suggestions on how this effort can be carried beyond the initial analysis.

5.1. Changing Perspectives on the Discrete Aurora Phenomenon

In many aspects, the new MAVEN/IUVS observations confirm and reinforce the results from MEx/SPICAM. First and foremost, the connection between discrete auroral and crustal fields is confirmed and extended. The new data set goes beyond an association between the two by revealing a continuum from the brightest, most frequent events near the strongest fields down to rare, faint events near field strengths lower by orders of magnitude. Many of the characteristics of the new events are also similar, such as altitudes, emission properties and minimum durations while offering the chance for improved statistical studies.

In other aspects, the new data set fundamentally alters our perspective on the discrete aurora phenomenon. We now know it is fairly widespread on Mars, thanks to IUVS's higher sensitivity and substantially higher observation duty cycle. Discrete aurora can happen almost anywhere on Mars (not just in the strong crustal field region) and are observed nearly 1% of the time globally. The expanded observations dispel perception that the events are rare and fleeting. Instead, discrete aurora in the strong crustal field should be seen as likely every evening when IMF conditions are favorable, with displays lasting for hours. This argues that observations with different instruments are more likely to succeed and merit the effort. It further suggests that

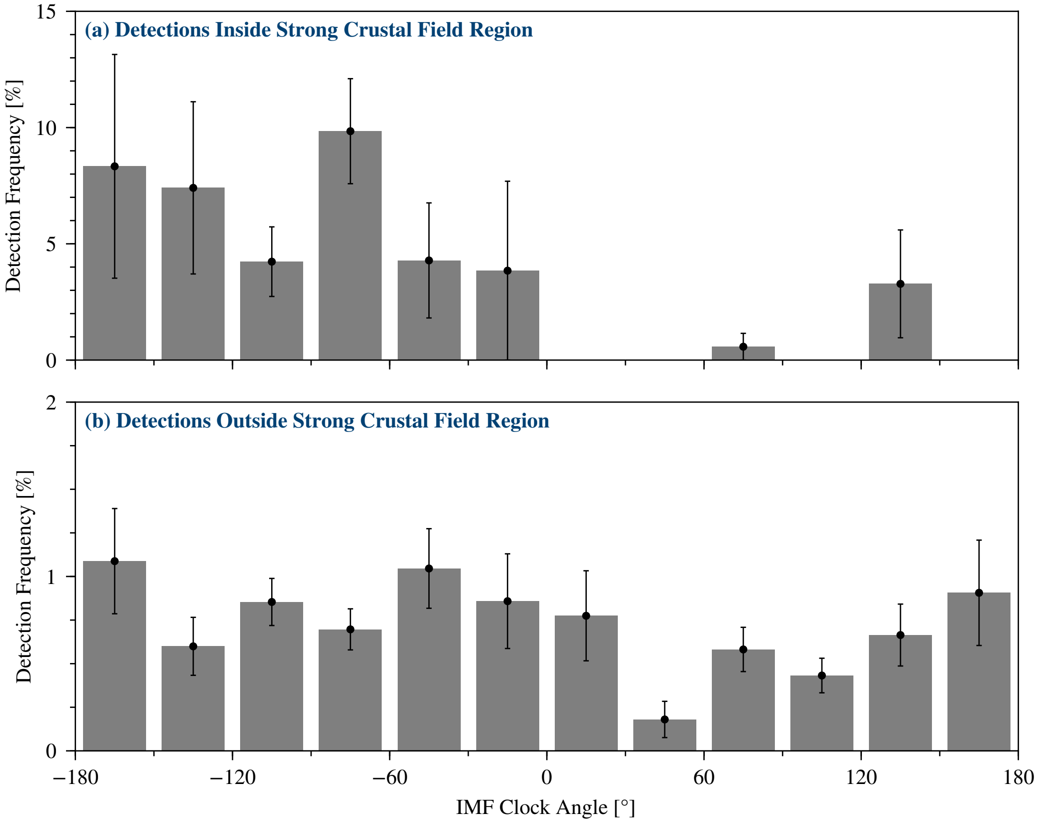

Figure 10. Detection frequency versus interplanetary magnetic field (IMF) clock angle. Inside the strong crustal region, nearly all events occur when the clock angle is negative, which indicates the B_y component of the IMF is negative.

astronauts, whenever they reach Mars, would have a good chance to see this natural wonder from above or below (Lilensten et al., 2015, Soret21).

5.2. Insights Into the Causes of Discrete Aurora

Discrete aurora events are spatially confined and have some association with the Martian crustal magnetic fields. It is therefore tempting to ascribe the same auroral formation mechanism that is known to operate in Earth's magnetosphere: parallel potential structures are established on field lines that connect to the collisional atmosphere, and electrons are accelerated downward toward the atmosphere in these potentials, resulting in auroral emission. There is evidence from both MAVEN particle and field measurements and from previous spacecraft measurements that this mechanism operates at Mars. Accelerated electron energy distributions have been measured above Martian crustal fields (Brain, Halekas, et al., 2006; Lundin et al., 2006; Xu et al., 2020), magnetic field perturbations consistent with field-aligned currents have been observed near cusp regions (Brain, Halekas, et al., 2006), and upward accelerated ions have been observed in the same locations as energized electrons (possibly consistent with the existence of parallel potentials above Martian cusps) (Lundin et al., 2006). It therefore seems likely that similar mechanisms accelerate electrons into the atmospheres of Mars and Earth, on different spatial scales. One caveat is that field-aligned potentials at Earth are located on closed magnetic field lines that connect to the plasma sheet on the nightside of the planet. At Mars, the evidence for field-aligned potentials occurs on both closed and open magnetic field lines, but almost always near the boundary between the two topologies. Using the known physics from Earth's auroral system, we offer the following explanation.

Depending on solar wind IMF orientation, the draped magnetic field at Mars can be roughly opposite to a local crustal field direction. Indeed, the topology of Martian crustal magnetic fields depends upon the IMF clock angle (Brain et al., 2020; Weber et al., 2020), explaining the strong dependence of auroral detections on IMF orientation described in Section 4.3. The interface between these oppositely directed magnetic fields will have strong currents perpendicular to B (carried by pressure gradients) that can be unstable to reconnection. Reconnection to crustal fields (Harada et al., 2018) produces open flux tubes that form part of the Martian magnetotail, with the bulk of the magnetotail resulting from draped IMF. As open flux tubes rotate to the nightside, the ionospheric source of magnetotail plasma on those open flux tubes is reduced. When the cross-tail currents can no longer be maintained by stable pressure gradients, reconnection will occur, producing closed crustal flux tubes that relax (dipolarize) to their unperturbed geometry. This reconnection, associated with a drop in ionospheric source plasma, explains the increased probability of aurora in the post-dusk crustal field sector.

Reconnection will result in flux tubes that interchange with other crustal flux tubes, producing vortex flows (Birn et al., 2004) with associated electric fields and field-aligned currents (FACs) that map to the ionosphere just like the Earth system. As in the Earth system, the high altitude FACs connect through Pedersen currents in the ionosphere (Cowley, 2000). Pedersen currents are perpendicular to the magnetic field and result from finite plasma resistivity due to collisions with neutrals. The finite resistivity produces a positive $\boldsymbol{J}\cdot\boldsymbol{E}$, and therefore dissipation in the system. The free energy available from interchanging flux tubes is dissipated in the ionosphere as the flux tubes relax to their unperturbed crustal configuration.

As with the Earth system, parallel electric fields form as necessary to maintain the FACs. Generally, these parallel electric fields can be small for highly conducting plasmas. However, as with the Earth system, the interface between ionosphere and magnetosphere is the bottleneck where the plasma requires the largest electric fields (Ergun et al., 2002). For large enough FACs, the required electric fields can be a kilovolt or more. In the Earth system, these regions of parallel electric field (or parallel potential drops) produce the brightest auroral arcs and the inverted-V signatures seen in electron spectrograms (Frank & Ackerson, 1971; McFadden et al., 1999). A similar formation of parallel electric fields is believed to play a role in Martian aurora producing inverted-V signatures such as those reported by Xu et al. (2020).

A number of questions present themselves from the UV observations that may challenge this interpretation. First, both the frequency and brightness of the observed aurora depend upon the strength of the radial component of the magnetic field. Is this consistent with an Earth-like auroral mechanism? Higher frequency of aurora in stronger magnetic fields could mean that potential structures are more readily established in strong magnetic cusps, or that the potentials established in strong field regions more often result in detectable auroral emission. Strong field regions should have more spatially confined cusps at the altitudes where emission occurs, resulting in brighter aurora for the same incident flux of particles.

Second, a large number of the auroral detections occur far from crustal magnetic fields. How can this be explained using an Earth-like auroral formation mechanism? We first note that auroral-like electron distributions have also been observed far from crustal fields (Brain, Halekas, et al., 2006; Halekas et al., 2008), and that the electron distributions far from crustal fields are more likely to be spatially extended (Halekas et al., 2008). MAVEN observations have also revealed that the magnetic topology at low altitudes near Mars is quite complex, with crustal magnetic fields lines extending far from their geographic region of origin (Xu et al., 2017). Thus, it is conceivable that electrons can be accelerated on crustal magnetic field lines as described above, yet still cause emission far from crustal fields if there is magnetic connection to a crustal field region.

Finally, a long-standing question for Martian discrete aurora has been whether they are long-lived on timescales of hours. Theoretical arguments (Dubinin et al., 2008) suggest that the conductivity of the Martian nightside ionosphere is sufficiently high that potential structures cannot be maintained for very long. Our explanation of discrete aurora earlier in this section suggests that aurora are active post-dusk, and subside as crustal fields rotate through the night side. Yet, observations of accelerated electron distributions in the same crustal field region on several successive orbits (Dubinin et al., 2009) suggest that the aurora can indeed be long-lived or at least repeat with each rotation of Mars. Recent models of Martian cusps have employed kinetic assumptions to examine whether potential structures can be formed and maintained (Poppe et al., 2020). These models demonstrate that even for relatively basic assumptions about cusp morphology and the interacting magnetospheric and ionospheric particle populations that steady-state potential structures can be formed. The results we present here support these findings, as aurora in the strongest crustal field regions appear to persist during evening hours for extended periods of time (see Section 4.3).

5.3. Future Work

This initial analysis of IUVS discrete aurora observations opens the door to many deeper studies. First, the automated statistical detection algorithm could be significantly improved by including substantially more pixels. The single-pixel SNR > 4 cutoff used in this work does not take advantage of probable good signal in neighboring pixels. These could be coadded to obtain higher overall SNR and better spatial information. Expanding pixel coverage will be especially valuable for the simultaneous FUV observations not used in this study due to their lower SNR. Second, deeper correlation studies between the causal factors (local time, IMF clock angle, B_r), along with studies of non-detections, may yield clearer insights into the mechanisms driving auroral acceleration and precipitation. Correlating events with the solar wind dynamic pressure might give additional clues. Third, the study of individual events offers a rich variety of local and external magnetospheric conditions and viewing geometries. The individual morphologies of the observed emissions (see Figure 4) may also give clues to where precipitation is occurring. Fourth, further investigations into the contemporaneous SWEA electron measurements should help constrain the flux and energy and thereby give insights into the acceleration mechanisms (e.g., Xu et al., 2020; Soret21). Fifth, modeling efforts will be key to understanding how the complex and dynamic combination of Mars' magnetic and charged particle conditions cause this phenomenon. Lastly, collaborative studies with the EMUS ultraviolet instrument on the Emirates Mars Mission (El-Showk, 2020), are likely to benefit from their complementary capabilities.

Data Availability Statement

The data may be obtained from the Planetary Atmospheres Node of the Planetary Data System using the filenames and version numbers in the text. This work used high-level data products (MLR brightnesses derived from PDS products) which will be archived in the FAIR-compliant CU Scholar Repository at https://doi.org/10.25810/2a0h-9w11.

Acknowledgments
The MAVEN mission is supported by NASA in association with the University of Colorado and NASA's Goddard Space Flight Center. This project acknowledges funding from BELSPO, with financial and contractual coordination by the ESA PRODEX Office (PEA grant numbers 4000103401 and 4000121493).

References

Bertaux, J., Leblanc, F., Witasse, O., Quemerais, E., Lilensten, J., Stern, S. A., et al. (2005). Discovery of an Aurora on Mars. *Nature*, *435*(7043), 790–794. https://doi.org/10.1038/nature03603

Birn, J., Raeder, J., Wang, Y. L., Wolf, R. A., & Hesse, M. (2004). On the propagation of bubbles in the geomagnetic tail. *Annales Geophysicae*, *22*(5), 1773–1786. https://doi.org/10.5194/angeo-22-1773-2004

Brain, D. A., Lillis, R. J., Mitchell, D. L., Halekas, J. S., & Lin, R. P. (2007). Electron pitch angle distributions as indicators of magnetic field topology near Mars. *Journal of Geophysical Research*, *112*, A09201. https://doi.org/10.1029/2007JA012435

Brain, D. A., Halekas, J. S., Peticolas, L. M., Lin, R. P., Luhmann, J. G., Mitchell, et al. (2006). On the origin of aurorae on Mars. *Geophysical Research Letters*, *33*(L01201). https://doi.org/10.1029/2005GL024782

Brain, D. A., Mitchell, D. L., & Halekas, J. S. (2006). The magnetic field draping direction at Mars from April 1999 through August 2004. *Icarus*, *182*(2), 464–473. https://doi.org/10.1016/j.icarus.2005.09.023

Brain, D. A., Weber, T., Xu, S., Mitchell, D. L., Lillis, R. J., Halekas, J. S., et al. (2020). Variations in nightside magnetic field topology at Mars. *Geophysical Research Letters*, *47*, e2020GL088921. https://doi.org/10.1029/2020GL088921

Connerney, J. E. P., Espley, J., Lawton, P., Murphy, S., Odom, J., Oliversen, R., & Sheppard, D. (2015). The MAVEN magnetic field investigation. *Space Science Reviews*, *195*, 257–291. https://doi.org/10.1007/s11214-015-0169-4

Connerney, J. E. P., Espley, J. R., DiBraccio, G. A., Gruesbeck, J. R., Oliversen, R. J., Mitchell, D. L., et al. (2015). First results of the MAVEN magnetic field investigation. *Geophysical Research Letters*, *42*, 8819–8827. https://doi.org/10.1002/2015GL065366

Cowley, S. W. H. (2000). Magnetosphere-ionosphere interactions: A tutorial review. In S.-I. Ohtani, R. Fujii, M. Hesse, & R. L. Lysak (Eds.), *Magnetospheric current systems*. https://doi.org/10.1029/GM118p0091

Deighan, J., Jain, S. K., Chaffin, M. S., Fang, X., Halekas, J. S., Clarke, J. T., et al. (2018). Discovery of proton aurora at Mars. *Nature Astronomy*, *2*, 802–807. https://doi.org/10.1038/s41550-018-0538-5

DiBraccio, G. A., Luhmann, J. G., Curry, S. M., Espley, J. R., Xu, S., Mitchell, D. L., et al. (2018). The twisted configuration of the Martian magnetotail: MAVEN observations. *Geophysical Research Letters*, *45*, 4559–4568. https://doi.org/10.1029/2018GL077251

Dubinin, E., Chanteur, G., Fraenz, M., & Woch, J. (2008). Field-aligned currents and parallel electric field potential drops at Mars. Scaling from the Earth' aurora. *Planetary and Space Science*, *56*(6), 868–872. https://doi.org/10.1016/j.pss.2007.01.019

Dubinin, E., Fraenz, M., Woch, J., Barabash, S., & Lundin, R. (2009). Long-lived auroral structures and atmospheric losses through auroral flux tubes on Mars. *Geophysical Research Letters*, *36*(8), 08108. https://doi.org/10.1029/2009GL038209

El-Showk, S. (2020). *Science*, *369*, 127. https://doi.org/10.1126/science.369.6500.127

Ergun, R. E., Andersson, L., Main, D., Su, Y., Newman, D. L., Goldman, M. V., et al. (2002). Parallel electric fields in the upward current region of the aurora: Numerical solutions. *Physics of Plasmas*, *9*(9), 3695–3704. https://doi.org/10.1063/1.1499121

Frank, L. A., & Ackerson, K. L. (1971). Observations of charged particle precipitation into the auroral zone. *Journal of Geophysical Research*, *76*(16), 3612–3643. https://doi.org/10.1029/JA076i016p03612

Gérard, J.-C., Soret, L., Libert, L., Lundin, R., Stiepen, A., Radioti, A., & Bertaux, J.-L. (2015). Concurrent observations of ultraviolet aurora and energetic electron precipitation with Mars Express. *Journal of Geophysical Research: Space Physics*, *120*, 6749–6765. https://doi.org/10.1002/2015ja021150

Halekas, J. S., Brain, D. A., Lin, R. P., Luhmann, J. G., & Mitchell, D. L. (2008). Distribution and variability of accelerated electrons at Mars. *Advances in Space Research*, *41*(9), 1347–1352. https://doi.org/10.1016/j.asr.2007.01.034

Halekas, J. S., Brain, D. A., Luhmann, J. G., DiBraccio, G. A., Ruhunusiri, S., Harada, Y., et al. (2017). Flows, fields, and forces in the Mars-solar wind interaction. *Journal of Geophysical Research: Space Physics*, *122*, 11320–11341. https://doi.org/10.1002/2017JA024772

Harada, Y., Halekas, J. S., DiBraccio, G. A., Xu, S., Espley, J., McFadden, J. P., et al. (2018). Magnetic reconnection ON dayside crustal magnetic fields at Mars: MAVEN Observations. *Geophysical Research Letters*, *45*(10), 4550–4558. https://doi.org/10.1002/2018gl077281

Hurley, D. M., Dong, Y., Fang, X., & Brain, D. A. (2018). A proxy for the upstream IMF clock angle using MAVEN magnetic field data. *Journal of Geophysical Research: Space Physics*, *123*, 9612–9618. https://doi.org/10.1029/2018JA025578

Jain, S. K., Stewart, A. I. F., Schneider, N. M., Deighan, J., Stiepen, A., Evans, J. S., et al. (2015). The structure and variability of Mars upper atmosphere as seen in MAVEN/IUVS dayglow observations. *Geophysical Research Letters*, *42*, 9023–9030. https://doi.org/10.1002/2015GL065419

Jakosky, B. M., Grebowsky, J. M., Luhmann, J. G., Connerney, J., Eparvier, F., Ergun, R., et al. (2015). MAVEN observations of the response of Mars to an interplanetary coronal mass ejection. *Science*, *350*(6261). https://doi.org/10.1126/science.aad0210

Jakosky, B. M., Lin, R. P., Grebowsky, J. M., Luhmann, J. G., Mitchell, D. F., Beutelschies, G., et al. (2014). The Mars atmosphere and volatile evolution (MAVEN). *Space Science Reviews*, *195*, 3–48. https://doi.org/10.1007/s11214-015-0139-x

Leblanc, F., Witasse, O., Lilensten, J., Frahm, R. A., Safaenili, A., Brain, D. A., et al. (2008). Observations of aurorae by SPICAM ultraviolet spectrograph on board Mars Express: Simultaneous ASPERA-3 and MARSIS measurements. *Journal of Geophysical Research*, *113*(A08311). https://doi.org/10.1029/2008JA013033

Leblanc, F., Witasse, O., Winningham, J., Brain, D., Lilensten, J., Blelly, P.-L., et al. (2006). Origins of the Martian aurora observed by spectroscopy for investigation of characteristics of the atmosphere of Mars (SPICAM) on board Mars Express. *Journal of Geophysical Research*, *111*(A09313). https://doi.org/10.1029/2006JA011763

Lilensten, J., Bernard, D., Barthélémy, M., Gronoff, G., Wedlund, C. S., & Opitz, A. (2015). Prediction of blue, red and green aurorae at Mars. *Planetary and Space Science*, *115*, 48–56. https://doi.org/10.1016/j.pss.2015.04.015

Lundin, R., Winningham, D., Barabash, S., Frahm, R., Holmström, M., Sauvaud, J.-A., et al. (2006). Plasma acceleration above Martian magnetic anomalies. *Science*, *311*(5763), 980–983. https://doi.org/10.1126/science.11220710.1126/science.1122071

McClintock, W. E., Schneider, N. M., Holsclaw, G. M., Hoskins, A. C., Stewart, I., Deighan, J., et al. (2015). The Imaging Ultraviolet Spectrograph (IUVS) for the MAVEN mission. *Space Science Reviews*, *195*, 75–124. https://doi.org/10.1007/s11214-014-0098-7

McFadden, J. P., Carlson, C. W., & Ergun, R. E. (1999). Microstructure of the auroral acceleration region as observed by fast. *Journal of Geophysical Research*, *104*(A7), 14453–14480. https://doi.org/10.1029/1998ja900167

Poppe, A. R., Brain, D. A., Dong, Y., Xu, S., & Jarvinen, R. (2020). Particle-in-cell modeling of Martian magnetic cusps and their role in enhancing nightside ionospheric ion escape. *Geophysical Research Letters*, *48*, e2020GL090763. https://doi.org/10.1029/2020GL090763

Ritter, B., Gérard, J.-C., Hubert, B., Rodriguez, L., & Montmessin, F. (2018). Observations of the proton aurora on Mars with SPICAM on board Mars Express. *Geophysical Research Letters*, *45*, 612–619. https://doi.org/10.1002/2017GL076235

Schneider, N. M., Deighan, J. I., Jain, S. K., Stiepen, A., Stewart, A. I. F., Larson, D., et al. (2015). Discovery of diffuse aurora on Mars. *Science*, *350*(6261). https://doi.org/10.1126/science.aad0313

Schneider, N. M., Deighan, J. I., Stewart, A. I. F., McClintock, W. E., Jain, S. K., Chaffin, M. S., et al. (2015). MAVEN IUVS observations of the aftermath of the Comet Siding Spring meteor shower on Mars. *Geophysical Research Letters*, *42*, 4755–4761. https://doi.org/10.1002/2015GL063863

Schneider, N. M., Jain, S. K., Deighan, J., Nasr, C. R., Brain, D. A., Larson, D., et al. (2018). Global aurora on Mars during the September 2017 space weather event. *Geophysical Research Letters*, *45*, 7391–7398. https://doi.org/10.1029/2018GL077772

Schneider, N. M., Milby, Z., Jain, S. K., González-Galindo, F., Royer, E., Gérard, J.-C., et al. (2020). Imaging of Martian circulation patterns and atmospheric tides through MAVEN/IUVS nightglow observations. *Journal of Geophysical Research: Space Physics*, *125*. https://doi.org/10.1029/2019JA027318

Soret, L., Gérard, J.-C., Libert, L., Shematovich, V. I., Bisikalo, D. V., Stiepen, A., & Bertaux, J.-L. (2016). SPICAM observations and modeling of Mars aurorae. *Icarus*, *264*, 398–406. https://doi.org/10.1016/j.icarus.2015.09.023

Soret, L., Gérard, J.-C., Schneider, N., Jain, S., Milby, Z., Ritter, B., et al. (2021). Discrete aurora on Mars: Spectral properties, vertical profiles, and electron energies. *Journal of Geophysical Research: Space Physics*, *126*, e2021JA029495. https://doi.org/10.1029/2021JA029495

Stevens, M. H., Evans, J. S., Schneider, N. M., Stewart, A. I. F., Deighan, J., Jain, S. K., et al. (2015). New observations of molecular nitrogen in the Martian upper atmosphere by IUVS on MAVEN. *Geophysical Research Letters*, *42*, 9050–9056. https://doi.org/10.1002/2015GL065319

Stiepen, A., Jain, S. K., Schneider, N. M., Deighan, J. I., González-Galindo, F., Gérard, J.-C., et al. (2017). Nitric oxide nightglow and Martian mesospheric circulation from MAVEN/IUVS observations and LMD-MGCM predictions. *Journal of Geophysical Research: Space Physics*, *122*, 5782–5797. https://doi.org/10.1002/2016JA023523

Weber, T., Brain, D., Xu, S., Mitchell, D., Espley, J., Halekas, J., et al. (2020). The influence of interplanetary magnetic field direction on Martian crustal magnetic field topology. *Geophysical Research Letters*, *47*, e2020GL087757. https://doi.org/10.1029/2020GL087757

Weber, T. D. (2020). *The role of crustal magnetic fields in atmospheric escape from mars (Order No. 28149912)*. Retrieved from Available from ProQuest Dissertations & Theses Global. (2474837751) https://www.proquest.com/dissertations-theses/role-crustal-magnetic-fields-atmospheric-escape/docview/2474837751/se-2?accountid=14667

Wilcox, J. M., & Ness, N. F. (1965). Quasi-stationary corotating structure in the interplanetary medium. *Journal of Geophysical Research*, *70*(23), 5793–5805. https://doi.org/10.1029/JZ070i023p05793

Xu, S., Mitchell, D., Liemohn, M., Fang, X., Ma, Y., Luhmann, J., et al. (2017). Martian low-altitude magnetic topology deduced from MAVEN/SWEA observations. *Journal of Geophysical Research*, *122*(2), 1831–1852. https://doi.org/10.1002/2016JA023467

Xu, S., Mitchell, D. L., McFadden, J. P., Fillingim, M. O., Andersson, L., Brain, D. A., et al. (2020). Inverted-V electron acceleration events concurring with localized auroral observations at Mars with MAVEN. *Geophysical Research Letters*, *47*, e2020GL087414. https://doi.org/10.1029/2020GL0874110.1029/2020gl087414